Inorganic Chemistry

pubs.acs.org/IC Article

Phase Discovery and Selected Synthesis of Subvalent Niobium Tellurides Using a Polytelluride Flux Strategy

Fan Sun, Haoyu Yue, Danilo Puggioni, Zhongnan Guo,* Yutong Li, James M. Rondinelli, Zheng Zhang, Wenxia Yuan,* and Mercouri G. Kanatzidis*



Cite This: Inorg. Chem. 2023, 62, 12413-12422



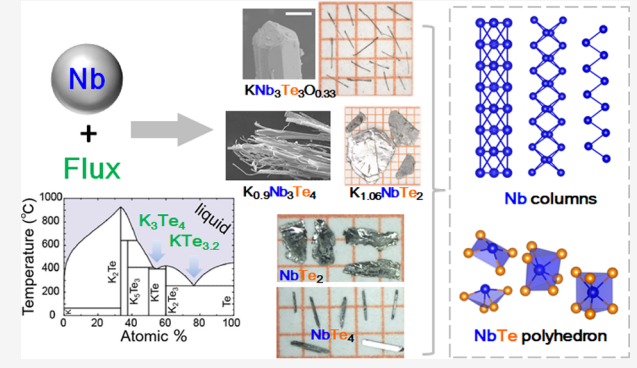
ACCESS I

Metrics & More

Article Recommendations

s Supporting Information

ABSTRACT: Transition metal subchalcogenides involve electronrich metals and can facilitate an in-depth understanding of the relationships among quantum properties such as superconductivity, charge density wave, and topological band structures. However, effective experimental routes toward synthesizing transition metal subchalcogenides are still lacking, hindering the development of new quantum materials. Herein, we propose a eutectic polytelluride flux strategy as an excellent solution to address phase discovery and crystal growth in transition metal subtelluride systems. We report new phases easily and selectively synthesized using a eutectic " K_3Te_4 " polytelluride flux upon adjusting the ratio of Nb metal to flux in the starting materials (K/Nb/Te = 3:x:4). Using a high Nb content in the solvent (x = 2 and 1), crystals of $KNb_3Te_3O_{0.38}$ and $K_{0.9}Nb_3Te_4$



are obtained. Both subtellurides exhibit diverse Nb clusters, including face-sharing and edge-sharing Nb₆ octahedral columns and zigzag Nb chains. Reducing the Nb content to x = 0.33 leads to the formation of a layered compound, $K_{1.06}$ NbTe₂. This compound comprises a NbTe₆ trigonal prism with K intercalated between the layers. Single crystals of known binary Nb tellurides can also be grown using another eutectic flux "KTe_{3.2}", and the obtained NbTe₂ exhibits a new polymorphism with extra trimerization along the b-axis in the Nb–Nb bonded double zig-zag cluster. Precise control over the structural dimensionality and oxidation state, combined with the facile crystal growth process, makes our synthetic strategy an efficient route to explore quantum materials in transition metal subchalcogenides.

■ INTRODUCTION

Metal-rich subvalent compounds have both metal-metal and metal-main group (such as oxide, chalcogenide, and halide) bonding interactions in their structures. In these compounds, the average valence state of the metal atoms is generally smaller than that expected from the N-8 rule. 1,2 Extraordinary structural chemistry and exotic physical properties are often observed in the subvalent compounds, which can be ascribed to the non-integer oxidation state of the metal atoms and low concentration of valence electrons. Over the past decade, subvalent materials, particularly those containing transition metals, have drawn considerable research attention because a variety of quantum properties have been discovered.^{3–10} K₂Cr₃As₃, with one-dimensional (1D) Cr octahedral clusters discovered by Bao et al., exhibits unconventional superconductivity.³ TlMo₃Se₃ with a similar 1D Mo octahedral column is considered as the topological superconductor with a Dirac cone near the Fermi level in its electronic band structure. 11,12 KMn₆Bi₅ which exhibits a unique 1D Mn pentagonal antiprism structure is an antiferromagnetic metal; it exhibits superconductivity when the antiferromagnetism is suppressed under high pressure.^{13,14} In addition to the 1D subvalent metal clusters, two-dimensional (2D) metallic motifs also exhibit interesting quantum properties. For example, a 2D metallic Kagome lattice, such as the ferromagnetic Weyl semimetal $\text{Co}_3\text{Sn}_2\text{S}_2$ and topological superconductors AV_3Sb_5 (A = K, Rb, and Cs), allows a combination of superconductivity, topological band structure, and charge density wave (CDW) to be achieved. Even in the well-studied transition metal dichalcogenides (TMDCs), the Weyl semimetal state, CDW, and superconductivity can be obtained in a distorted octahedral configuration with metal—metal bonding interactions in their structure. This suggests that subvalent features have formed in these layered binary compounds. The development of numerous compounds within this family of potential quantum materials depends on progress in new phase discovery and related synthetic chemistry.

Received: May 17, 2023 Published: July 25, 2023





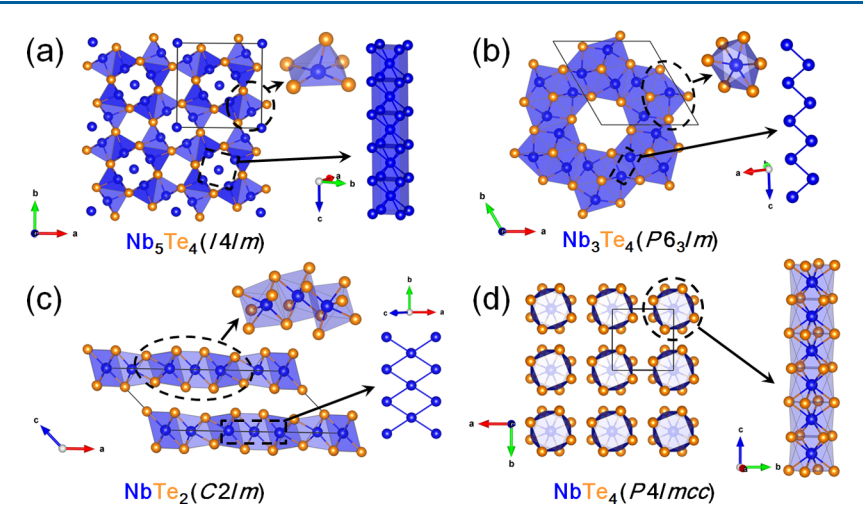


Figure 1. Crystal structures of the reported binary Nb tellurides observed in the Nb–Te binary system: (a) Nb_5Te_4 , (b) Nb_3Te_4 (c) $NbTe_2$, and (d) $NbTe_4$.

Subchalcogenides have not been extensively investigated when compared to oxides and halides. Particularly, transition metal-based compounds have recently been recognized as outstanding quantum materials that exhibit high carrier mobility, giant magnetoresistance, anomalous Hall effect, and topological surface states. 4,7,9,19 The potential application of metal chalcogenides in thermoelectrics, catalysts, and detectors is an exciting prospect. 15,20-22 Although polycrystalline subchalcogenides can be synthesized using a traditional solid-state reaction, the process of preparing large single crystals for quantum property characterization remains challenging. Therefore, more work needs to be done to fully comprehend the characteristics of metal subchalcogenides. The chemical vapor transport (CVT) method has been widely used to grow crystals of transition metal subchalcogenides, such as TlMo₃Se₃, Nb₃Te₄, and TMDCs (such as MoTe₂ and WTe₂), ²⁴⁻²⁷ but only thermodynamically stable phases can be obtained as products. The kinetically stable phases, with unusual structures, are often missed.

The flux synthesis paradigm is a promising method used to address many materials discovery bottlenecks. For example, alkali metal chlorides (such as NaCl, KCl, or their mixture) and main-group metals with low melting points (such as In, Pb, Sn, and Bi) can be used as fluxes to overcome the refractory properties of transition metals during the synthesis and crystal growth of new samples. 28-32 Recently, Zhou et al. demonstrated that the mixed hydroxide and halide flux could be an efficient solvent to synthesize a variety of new chalcogenides. 33-35 Alkali-metal polychalcogenides, which contain chalcogen-chalcogen bonding ligands (Qx2-) in their structures (Q = S, Se, and Te), have been proven to be a feasible flux for the discovery of chalcogenide materials. 36-38 In the synthesis process, raw transition metals are dissolved by molten alkali-metal polychalcogenides. By adjusting the composition (x) in Q_x^{2-} , the oxidation state of the metal can be controlled to achieve specific states. This concept has served as a source of inspiration for us to explore new phases and novel structures by utilizing polychalcogenide flux in transition metal subchalcogenides.

The Nb telluride system is a typical quantum material "library," which exhibits a combination of CDW, superconductivity, and topological band structures. ^{25,39,40} In this study, we selected Nb–Te as a representative system and

demonstrated that alkali metal polytelluride flux is a powerful tool for the exploratory synthesis and crystal growth of subvalent Nb tellurides. Our work indicates that utilizing the eutectic polychalcogenide flux strategy is an effective approach for generating subchalcogenides with unique structures within Nb telluride systems. Three new Nb tellurides (KNb₃Te₃O_{0.38}, $K_{0.9}Nb_3Te_4$, and $K_{1.06}NbTe_2$) were synthesized utilizing a "K₃Te₄" flux close to the eutectic melting point. KNb₃Te₃O_{0.38} and K_{0.9}Nb₃Te₄ are typical sub-chalcogenides; the former is composed of 1D face-sharing octahedral Nb6 clusters surrounded by Te nets. Conversely, the latter exhibits a unique structure containing both 1D edge-sharing Nb₆ octahedral columns and Nb zig-zag chains. K_{1.06}NbTe₂ is a K-intercalated TMDC with edge-sharing NbTe₆ trigonal prisms in the layers. By adjusting the Nb content in the starting materials, we were able to finely control the oxidation state of Nb in the final products, resulting in a precise, selective synthesis. Our resistivity measurements and DFT calculations indicated that $K_{0.9}Nb_3Te_4$ and $K_{1.06}NbTe_2$ are semimetals with large band dispersions, and KNb3Te3O0.38 showed semiconductor-like behavior in low-temperature ranges (<29 K) and flat bands near Fermi level. Single crystals of binary Nb tellurides can also be selectively synthesized using the eutectic flux "KTe_{3.2}". In addition, a new polymorph of NbTe₂ was observed using single-crystal X-ray diffraction (SCXRD), in which the structure obtained from the flux method revealed further distortion of the Nb coordination environment compared to that obtained by the CVT route.

■ RESULTS AND DISCUSSION

First, it is useful to provide a brief review of the known Nb—Te binary and K—Nb—Te ternary systems reported to date. An experimental description of the Nb—Te binary phase diagram, which contains four binary Nb tellurides (namely, Nb₅Te₄, Nb₃Te₄, NbTe₂, and NbTe₄), was recently published. Figure 1a shows that subvalent Nb₅Te₄ is composed of an edgesharing NbTe₅ pyramid with Nb₉ centered-cubic clusters forming 1D face-sharing columns in its structure. Nb₃Te₄ is also a subchalcogenide, which exhibits a 1D structure with distorted NbTe₆ octahedra connected by edge- and face-sharing types, forming very large 1D channels (Figure 1b). Nb—Nb dimers can be observed in two edge-sharing octahedra, thus leading to the formation of Nb zig-zag chains

parallel to the c-axis. NbTe2, a member of the 2D TMDC family, adopts a layered structure with stacked edge-sharing NbTe₆ octahedra (Figure 1c). 44 Despite the +4 oxidation state of Nb obtained from its chemical formula, the Nb atoms are trimerized into Nb double zig-zag chains along the b-axis, thus suggesting that NbTe2 is also subvalent with metallic bonds in its structure. With the content of Nb decreased, the Nb-Nb bonds are also elongated from Nb₅Te₄ (2.909 and 2.948 Å), Nb_3Te_4 (2.973 Å) to $NbTe_2$ (3.33 Å). Finally, 1D $NbTe_4$ is composed of NbTe₈ square antiprisms that are face-connected in columns (Figure 1d).⁴⁵ Moreover, the Nb-Nb metallic bonds are no longer observed in NbTe4 because of the high concentration of Te in this compound. Notably, a Nb-rich phase comprising of Nb₃Te, which exhibits a β -W-type structure, can only be synthesized via a high-pressure route. Hence, it is not located in the thermodynamic phase diagram. 46 For K-Nb-Te ternary systems, only K_xNb₃Te₄ has been reported. It is obtained by intercalating potassium into the empty channels of the binary Nb₃Te₄ precursor with the original P6₃/m structure and unchanged Nb-Nb bonds.⁴⁷

Synthesis of Ternary K–Nb–Te Systems. In this study, the potassium polytelluride flux serves as both the reagent and solvent, enabling the oxidation of Nb metal into the desired oxidation state. Figure 2a displays the K–Te binary phase

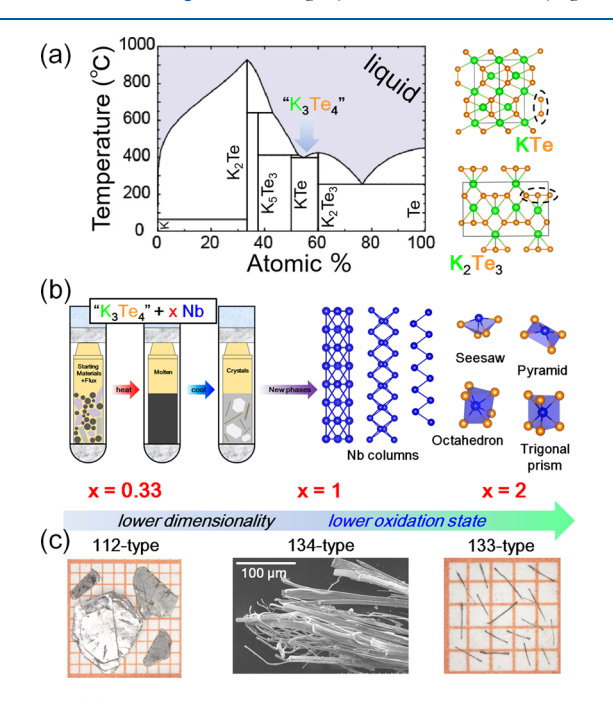


Figure 2. (a) K—Te binary phase diagram obtained from the database of Factsage 8.1 software⁴⁸ and the structure of KTe and K_2Te_3 . The composition of the " K_3Te_4 " flux is marked in the phase diagram, which is close to the eutectic melting point of KTe and K_2Te_3 . (b) Schematic of the synthetic route used in this work to obtain diverse subvalent Nb clusters and NbTe polyhedra in newly discovered tellurides. (c) Optical photograph and SEM image of the product prepared from starting materials with x = 0.33, 1, and 2.

diagram, illustrating the occurrence of KTe and K_2Te_3 , which contain Te-Te dimers and Te-Te-Te trimers, respectively. The synthesis process utilizes these Te-Te bonds to partially oxidize the Nb metal. To obtain subvalent Nb tellurides with a lower Nb-oxidation state, thus it is advisable to avoid using a Te-rich flux with numerous Te-Te bonds. Given the high melting point of Nb metal, we chose a flux composition close

to the eutectic point (K0.45Te0.55@396 °C), labeled " K_3 Te4" for our synthesis. Subsequently, an exploratory synthesis was performed using a molar ratio of K/Nb/Te = 3:x:4, and a detailed description of the synthetic method is provided in the experimental section of the Supporting Information. Presynthesis of potassium polytelluride flux as a precursor was not required to obtain the ternary phase. Therefore, K ingots and Te pellets were directly added to the crucible for the reaction, as shown in Figures 2b and S1. This significantly shortened the reaction time and reduced the number of variables.

A variety of crystals can be obtained by adjusting the xvalues in the starting materials. Figure 2c shows that when x =2, the products obtained are black needle-like crystals. Scanning electron microscopy (SEM) image revealed that the crystals are approximately 2 mm in length with hexagonal prism morphology. On reducing the x value to 1, the hexagonal prisms disappear and very thin ribbon-shaped crystals with lengths <1 mm are observed in the product. Although both crystals exhibit 1D features, the ribbon-shaped crystals can be easily distinguished from the hexagonal prisms during SEM analysis (Figure S2). When x is further decreased to 0.33, plate-like crystals with a metallic luster are obtained. Composition analysis of the three types of crystals is performed on their fresh surfaces using X-ray energy dispersive spectroscopy (EDS) and the results confirm the ternary nature of these three types of crystals with a chemical ratio of K/Nb/ Te = 1:3:3, 1:3:4, and 1:1:2 for the 1D prism (x = 2), 1D ribbon (x = 1), and 2D plate (x = 0.33) samples, respectively (Figure S3). Elemental mapping confirmed the homogeneous distribution of K, Nb, and Te in all three samples.

Crystal Structures. SCXRD analysis was used to solve the structures of the three samples. Crystallographic data are listed in Tables S1–S9 in the Supporting Information. The hexagonal prism crystal (x = 2, denoted as the 133-type phase) was found to adopt a TlFe₃Te₃-type structure in the $P6_3/m$ space group with infinite $(Nb_3Te_3)_{\infty}$ chains formed along the c-axis (Figure 3a,b). The Nb clusters consist of

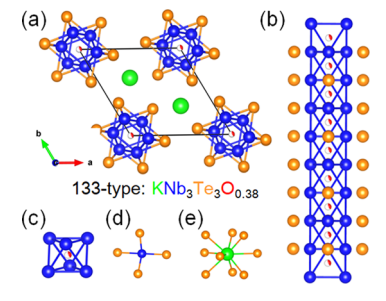


Figure 3. (a) Crystal structure of $KNb_3Te_3O_{0.38}$ viewed along the chain direction. (b) Side view of the double-wall nanowire structure. (c) V_6 octahedron with interstitial O. Chemical coordination of (d) V and (e) K.

stacked Nb₃ triangles with each triangle rotated 60° relative to its neighbor, thus forming face-sharing octahedral columns (Figure 3c). Notably, the same structural configuration of the 1D metal octahedral columns has been observed in Fe-, Mo-, Ni-, and V-based subvalent compounds in previous studies. However, the Nb₆ octahedral clusters observed here seem to be unique. Based on the average structure obtained from SCXRD, the Nb-Nb bond lengths are identical in the *ab* plane (2.996(1) Å), and comparable to those in elemental Nb (2.86 Å) (Figure S4). The comparable bond lengths indicate

the formation of Nb–Nb metallic bonds in the 1D subchalcogenide. The Nb–Nb distance between the different Nb₃ planes was 2.945(1) Å, which is shorter than that observed in the *ab* plane. Additionally, each Nb atom was coordinated to four telluride anions, thereby forming a NbTe₄ see-saw motif with Nb–Te bond distances of 2.930(1) and 2.897(1) Å, respectively (Figure 3d). Consequently, the Nb₆ octahedral (or Nb₃ triangle) clusters are surrounded by Te cladding, thus exhibiting a double-walled nanowire motif (Figure 3b). The K⁺ cations are coordinated to nine telluride anions in a tri-capped trigonal prism, thus separating the (Nb₃Te₃) $_{\infty}$ nanowires from each other (Figure 3e). The interactions between the different nanowires are negligible when considering the large distances between the nearest Te anions (4.151(1) Å).

Surprisingly, our SCXRD measurements revealed interstitial oxygen atoms with a partial occupation at the center of the Nb₆ octahedron. Thus, the final composition was determined to be KNb₃Te₃O_{0.38} for this 133-type phase. Interstitial oxygen is an unintentional effect that may originate from the oxidized surface of the raw materials (Nb powder and/or potassium ingot). We speculate that the incorporation of oxygen at the center site can stabilize the Nb₆ cluster octahedron by reducing the anti-bonding character, like the V-based 133 system described in our previous work.⁵² The interstitial oxygen atoms in the Nb6 octahedra resulted in trimerization along the chain direction in the local structure by defining a Nb₃ triangle as the monomer. The atomic pair distribution function (PDF) obtained from the synchrotron X-ray total scattering pattern reveals that the extracted G(r) functions collected at 300 K provide a better fit using the trimer model compared to the trimer-free model (Figure 4ab). The improved refinement of

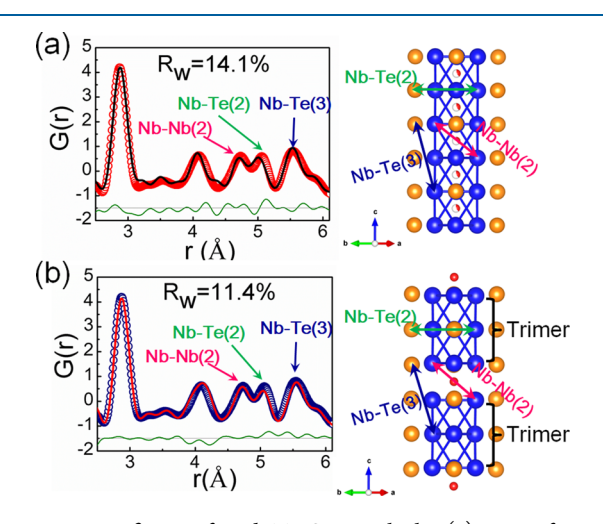


Figure 4. PDF fitting of KNb $_3$ Te $_3$ O $_{0.38}$ with the (a) trimer-free and (b) trimer model over the low r range (2.5–6.2 Å) at 300 K. The red and blue circles correspond to the experimental data, and the black and red lines represent the calculated data based on the structural models. The trimer-free and trimer structural models in the local range are shown on the right-hand side.

the peaks in the r range of 4.5–6 Å can be ascribed to the compressed Nb–Te(2) distance and elongated Nb–Te(3) distance in the trimer model, where Nb–Te(2) and Nb–Te(3) represent the second and third nearest neighboring Nb–Te pairs, respectively. This oxygen-induced local distortion is also observed in the V-based analog, $KV_3Te_3O_{\delta}$. The local trimerization in the Nb-based 133-type phase

persists over the temperature range from 400 to 87 K, as shown in the temperature-dependent PDF data in Figure S5.

The ribbon crystal (x = 1, denoted as the 134-type phase) exhibits a unique structure, as shown in Figure 5a. It

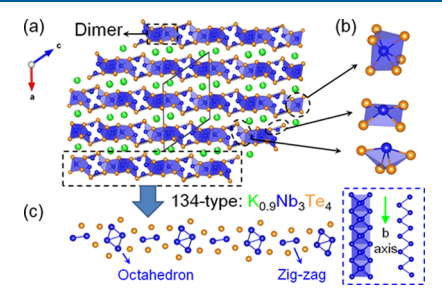


Figure 5. (a) Crystal structure of $K_{0.9}Nb_3Te_4$. (b) Three polyhedra in the structure including NbTe₆ octahedra, NbTe₄ pyramids, and NbTe₄ see-saws. (c) 1D Nb clusters formed along the *b*-axis in the structure.

crystallized in the monoclinic C2/m space group with lattice parameters of a = 18.238(10) Å, b = 3.591(2) Å, c = 15.339(9)Å, and $\beta = 123.997(18)^{\circ}$. The refined chemical formula is K_{0.9}Nb₃Te₄, which is consistent with the EDS results. Three types of polyhedra are observed in this structure: NbTe₆ octahedra, NbTe4 pyramids, and NbTe4 see-saws (Figure 5b). The NbTe₆ octahedron with an edge-sharing connection represents a dimer model and the Nb-Te bond lengths range between 2.742(7) and 2.941(7) Å, thus suggesting a highly distorted configuration. These (Nb₂Te₁₀) octahedral dimers are separated by two types of NbTe₄ polyhedra in layers: NbTe₄ see-saw face-shared with the octahedron with Nb-Te bond distances of 2.860(7) and 2.920(5) Å, and the NbTe₄ pyramid corner-shared with see-saw and edge-shared with each other with Nb-Te bond lengths of 2.793(4) and 2.777(6) Å. The K⁺ cations are partially occupied (refined as 0.90(1) from SCXRD) and intercalated between the layers in this structure. A very large displacement parameter of K is observed along the b-axis using SCXRD. This large parameter suggests that the alkali metal cations are highly disordered along this direction. It needs to be mentioned that the quality of K_{0.9}Nb₃Te₄ crystals is relatively low compared with the other two compounds, which can be implied by the much smaller size shown in Figure 2. In addition, the K_{0.9}Nb₃Te₄ crystals are very air sensitive and data collection was very challenging. The presence of high residuals and high weighted agreement factor during the refinement are presumably due to partial oxidative degradation of the crystals. Hence, we had to omit some bad reflections using the Olex2 program during the refinement.

Notably, two types of 1D Nb cluster columns are also formed in this 134-type phase. Figure 5c shows the Nb atoms in the pyramid and see-saw bond with each other, thus resulting in edge-sharing Nb₆ octahedral columns along the *b*-direction. Figure S4 shows that the octahedra are strongly compressed along the axial direction with an axial Nb–Nb distance of 2.907(10) Å. Moreover, compression led to long equatorial Nb–Nb distances of 3.591(3) and 4.122(9) Å. The Nb–Nb bond lengths from the pole to the equator are 3.115(6) and 3.077(4) Å, respectively (Figure S4). To the best of our knowledge, this edge-sharing Nb₆ octahedral cluster motif is unusual and has not been reported in other transition metal subchalcogenides to date. These edge-sharing Nb₆ octahedral columns are surrounded by Te anions, which

exhibit a 1D configuration like that of the 133-type structure (Figure S6). The Nb atoms in the dimeric (Nb₂Te₁₀) octahedra form zig-zag chains along the b-axis and the Nb–Nb bond length in this zig-zag motif is 3.089(7) Å, which is longer than that in Nb₃Te₄ (2.97 Å). These two types of 1D Nb clusters are arranged alternately in the layers, thus resulting in very strong in-plane anisotropy.

In terms of Nb clusters found in halides and chalcogenides, previous studies have shown that the Nb clusters in halides are typically isolated in the structures. These include the Nb₂ pairs in Nb₂I₈, the Nb₃ triangles in Nb₃I₈, and the Nb₆ octahedra in Nb₆I₁₁. The Nb clusters in the present compounds are all part of 1D type chains. These chains consist of face-sharing and edge-sharing Nb₆ octahedra, as well as Nb zig-zag chains. Additionally, we have observed that the unusual edge-sharing octahedral cluster structure present in $K_{0.9} \text{Nb}_3 \text{Te}_4$ has been observed in other metal sub-valence compounds, namely, $\text{Gd}_2 \text{Cl}_3$ and $\text{NbMo}_4 \text{O}_6$.

The 2D plate-like crystals obtained from the starting composition [K/Nb/Te = 3:0.33:4 (9:1:12)] crystallize in the hexagonal lattice $(P\overline{6}m2 \text{ space group})$ with lattice parameters of a = 3.666(2) and c = 10.145(7) Å. The structure can be considered as TMDC NbTe₂ with intercalated K (Figure 6a), wherein the structural motif is a NbTe₆ trigonal

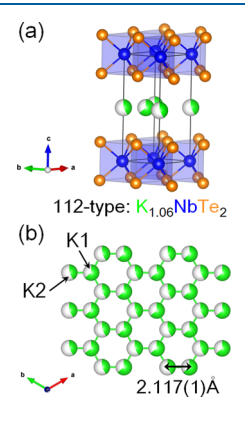


Figure 6. (a) Crystal structure of $K_{1.06}NbTe_2$. (b) The K honeycomb lattice with short K–K distance.

prism. This structure is different from the octahedral coordination observed in binary NbTe2. The Nb-Te bond length is determined to be 2.795(5) Å. K+ cations with a honeycomb structure are intercalated between the prismatic layers (Figure 6b). The SCXRD analysis reveals two Wyckoff positions for K in the structure with a partial occupation of 0.64 and 0.42, respectively, thus suggesting a chemical composition of K_{1.06}NbTe₂ for this layered phase. The distance between K(1) and K(2) is only 2.117(1) Å. This phenomenon has also been observed in some alkali-metal-intercalated metal sulfides and selenides. 57,58 Structural transformation from octahedral to trigonal prismatic coordination in NbTe2 after the intercalation of K can be expected as $K_{1.06}NbTe_2$ is isoelectronic to 2H-type MoTe₂ composed of a MoTe₆ trigonal prism.⁵⁹ Based on Rouxel's theory, Te-Te intralayer interactions (<4 Å) generally exist in transition metal ditellurides. These interactions lead to an overlap of the p orbitals of Te, and consequently, the electron transfer from the p orbitals of Te to the d orbitals of the transition metal.⁶⁰ Figure S7 shows that the Te-Te bonding distances in K_{1.06}NbTe₂ are longer than those in binary NbTe₂. This

implies that p-d electron transfer is weakened upon K intercalation.

By fixing the valence states of K and Te at +1 and -2, the oxidation states of Nb in the 133-, 134-, and 112-type phases were determined to be +1.92, +2.37, and +3, respectively. The precise tuning of the structural dimensionality and oxidation state of Nb in the final products was achieved by varying the ratio between Nb metal and the " K_3Te_4 " polytelluride flux, as clearly demonstrated. This suggests that the synthesis process allows for the precise selection of these subchalcogenides. In addition, we attempted to synthesize the three new Nb tellurides using the traditional solid—state reaction, but only the 133-type phase could be synthesized without flux, as shown in Figures S8 and S9. This highlights the ability of the eutectic polytelluride flux to access new synthesis pathways and kinetically stable compounds in transition metal tellurides.

Although we cannot entirely dismiss the possibility of hydrogen being present in our compounds, it is important to note that this is a common concern not only for our research but also for numerous other compounds described in the literature. The late John Corbett extensively addressed this issue and demonstrated that many compounds indeed contain hydrogen, which can contribute to their stability. ^{61–64} However, proving the existence of hydrogen requires extensive experimental work beyond the scope of this paper.

Electrical Resistivity Measurements. We give a brief description of the temperature-dependent resistivity for the $KV_3Te_3O_{0.38}$ and $K_{1.06}NbTe_2$ crystals (shown in Figure 7). The

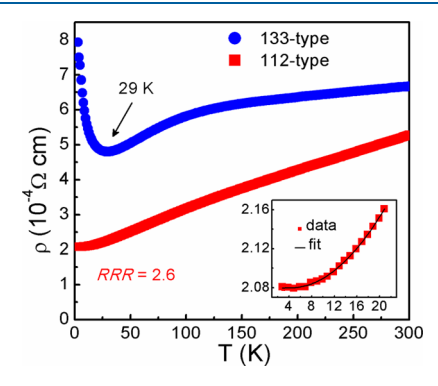


Figure 7. Temperature dependence of resistivity for KNb $_3$ Te $_3$ O $_{0.38}$ (133-type) and K $_{1.06}$ NbTe $_2$ (112-type) single crystals from 300 to 2 K. The data for K $_{1.06}$ NbTe $_2$ at low temperatures from 20 to 2 K are well-fitted with the formula $\rho(T)=\rho_0+AT^2$ (inset).

needle-like $KV_3Te_3O_{0.38}$ crystal exhibit a resistivity (ρ) of 6.66 \times 10⁻⁴ Ω cm at 300 K, which is comparable to those of other 133-type systems. 50,52 The resistivity exhibits metallic behavior at high temperatures (>29 K), below which ρ increases upon cooling. This semiconducting-like behavior below 29 K may be ascribed to defects and disorder in the crystals induced by the interstitial oxygen atoms. 52 The plate-like K_{1.06}NbTe₂ crystals exhibit metallic behavior over the complete temperature range studied, with a ρ value of 5.27 \times 10⁻⁴ Ω cm at 300 K. Linear behavior of ρ is observed from 300 to 100 K, and the residual resistivity ratio (RRR = $\rho(T = 300 \text{ K})/\rho(T = 2 \text{ K})$) is approximately 2.6. The data from 20 to 2 K show a T^2 dependence, which can be fitted using the equation $\rho(T) = \rho_0$ + AT^2 with the residual resistivity ρ_0 and the slope A as 207 $\mu\Omega$ cm and 0.0193 $\mu\Omega$ cm/K², suggesting a Fermi-liquid behavior. 65 It should be mentioned that the attempt to

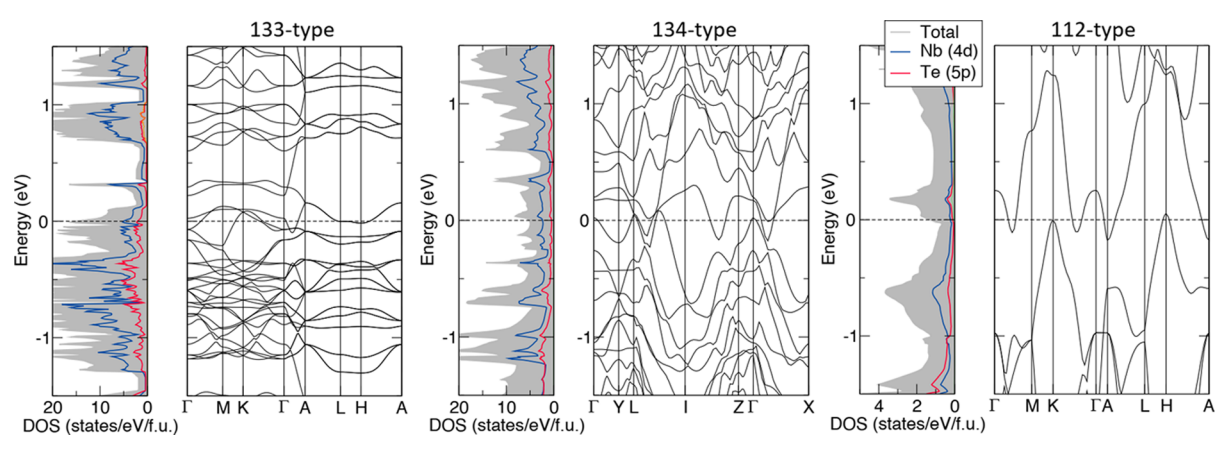


Figure 8. Calculated DOS and band structures of KNb₃Te₃O_{0,33} (133-type), K_{0,9}Nb₃Te₄ (134-type), and K_{1,06}NbTe₂ (112-type).

measure the resistivity of $K_{0.9}Nb_3Te_4$ failed in our lab due to the small size of the crystals.

Theoretical Electronic Structures. In Figure 8, we show the calculated densities-of-states (DOS) and band structures of $KNb_3Te_3O_{0.38}$ (133-type), $K_{0.9}Nb_3Te_4$ (134-type), and K_{1.06}NbTe₂ (112-type). Regardless of the chemical composition, the DOS shows strong hybridization between the Nb 4d and Te 5p states. The band structures of both K_{1.06}NbTe₂ and K_{0.9}Nb₃Te₄ indicate a semimetallic ground state with the former showing a larger band dispersion around the Fermi level. KNb₃Te₃O_{0.33} (133-type) exhibits quasi-1D metallic behavior with a larger number of states at the Fermi level than the other two compounds. Near the Fermi level, the bands are almost flat resulting in large effective masses. Moreover, the Fermi surface is nearly gapped along the A-L-H-A direction in the $k_z = 1/2$ plane. A small electron pocket exists along Γ -A. Hence, a small change in oxygen content (δ) will shift the chemical potential and the number of carriers available for transport. All the interesting features in resistivity and electronic bands require further characterizations in future studies (such as heat capacity, magnetism, and magnetoresistance), to deeply understand the novel behavior of these newly discovered compounds.

To understand the bond character of the Nb-clusters in these new compounds, we performed a crystal orbital Hamiltonian population (COHP) using the LOBSTER code. 66-69 The convention is to plot the negative COHP (-COHP, which is unitless) so that bonding interactions are positive, whereas antibonding interactions are negative, as shown in Figure S10. In KNb₃Te₃O_{0.38}, two different Nb₆ cluster octahedra are present: the oxygen-centered and the oxygen-free Nb-clusters. The COHP shows that the Nb-Nb bonds of the oxygen-centered Nb-cluster exhibit a nonbonding character, while the Nb-Nb bonds of the oxygen-free Nbcluster are strongly bonding at the Fermi level. This result confirms the stability of the 1D Nb telluride KNb₃Te₃O_{0,38}. In K_{0.9}Nb₃Te₄, at the Fermi level, the Nb–Nb bonds in the zigzag chain and the longer Nb-Nb bonds along the chain direction show nearly nonbonding character, while the Nb-Nb bonds within the ab plane exhibit strong bonding character. Conversely, the shorter Nb-Nb bonds along the chain exhibit antibonding character, leading to internal bond stresses and suggesting that local structural distortion may occur in this subtelluride. Lastly, the COHP of K_{1.06}NbTe₂ shows nearly nonbonding interaction near the Fermi level,

which is assigned to the absence of the Nb-cluster in this compound.

Formation of Binary Nb–Te Systems. Potassium is assumed to be incorporated into the product when K polychalcogenides are used as the flux in their synthesis. However, based on the concept reported in this study to control the oxidation state of Nb, binary Nb telluride with a relatively high valence state can be expected upon varying the composition of the flux toward being Te-rich. In this section, the composition of the flux is selected to be "KTe_{3.2}", which is close to another eutectic point (K0.24Te0.76@253 °C) on the Te-rich side of the K–Te binary system (Figure 9a). Two types of crystals are obtained upon varying the Nb content (x) in the starting materials (K/Nb/Te = 1:x:3.2). When x = 1, the product is plate-like crystal sheet, while when x is decreased to 0.6, the product is rod-shaped (Figure 9b). EDS measurements

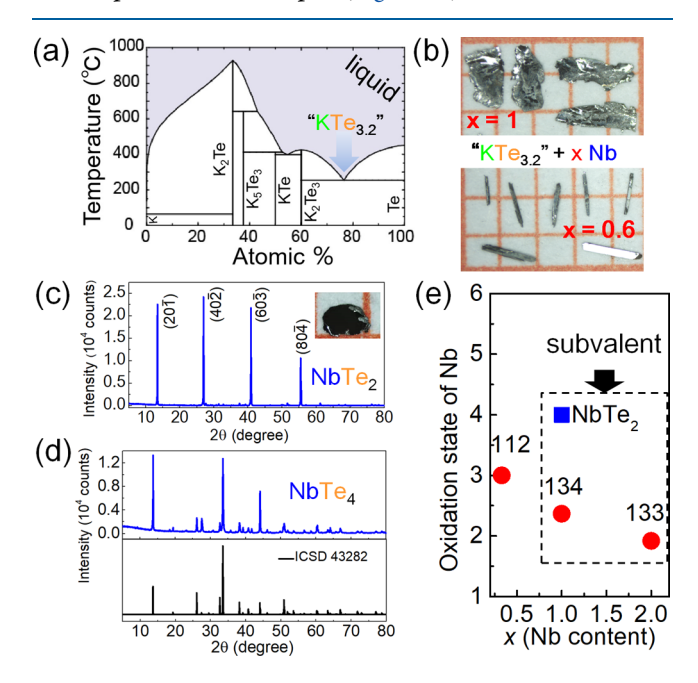


Figure 9. (a) Phase diagram of the K–Te binary system with "KTe_{3,2}" flux marked inside. (b) Optical photograph of the products with x=1 and 0.6. PXRD patterns obtained for the (c) NbTe₂ and (d) NbTe₄ crystals. (e) Relationship between the oxidation states of Nb in the final products and the Nb content (x) in the starting materials. It is noted that the NbTe₄ is not plotted here considering its polytelluride nature.

indicate that the products are binary compounds in the Nb-Te system, namely, NbTe₂ and NbTe₄ for x = 1 and 0.6, respectively, with a negligible amount of K in the samples (Figures S11 and S12). The crystal with x = 1 is easily exfoliated and the PXRD pattern of its cleaved surface reveals a highly preferred orientation (Figure 9c). The layer distance is calculated as ~6.62 Å, which is comparable to the data reported for binary NbTe2.44 This further confirms the successful synthesis of the K-free compound. The PXRD pattern of the ground rod crystals with x = 0.5 fits well with the pattern reported for NbTe₄ (ICSD 43282) (Figure 9d), further indicating the synthesis of this binary telluride. Based on the above results, the dependence of the Nb-oxidation state in the crystals on the Nb content in the starting materials is shown in Figure 9e (K₃Te₄ flux in red points and KTe_{3,2} in blue). It is evident that as the Nb content increases, the oxidation state of Nb in the products decreases. Additionally, KTe_{3,2} flux demonstrates a greater capacity to oxidize the transition metal. For the formation of a subchalcogenide with metalmetal interactions in its structure, the starting material's transition metal content relative to the flux used must be adequately high. This is noted that NbTe2 can be classified as a subtelluride, owing to the Nb-Nb bonding interactions present in its structure.

The fact that binary products exist in the Nb-Te system is well established. However, it is worth noting that this study presents a novel approach to growing single crystals of NbTe₂ using the flux method. The results of this study point to the value of alternative synthesis routes for stabilizing new polymorphs of other metal ditellurides. It is noteworthy that the NbTe₂ crystals produced in this study have a distinct structure from the NbTe2 synthesized through the CVT method as reported in the literature (denoted as C-NbTe₂). C-NbTe2 has been reported to exhibit a distorted octahedral configuration at room temperature with a double zig-zag chain motif along the b-axis.⁴⁴ Herein, two different Wyckoff positions for Nb are observed. The Nb(1) atoms are located in the center of the Nb cluster, thereby forming the middle string of the double zig-zag chain. Each Nb(1) atom is connected by four Nb(2) atoms, which form the outer strings of the double zig-zag chain (Figure 10). Based on the SCXRD, the crystal structure of NbTe2 obtained using flux method

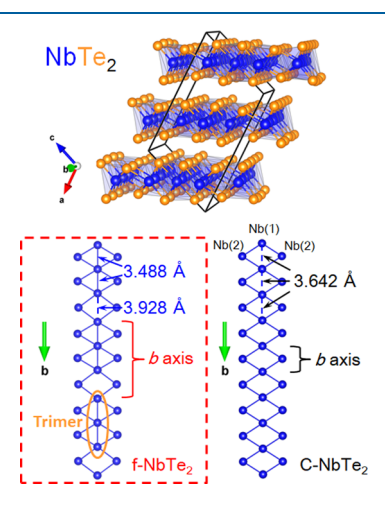


Figure 10. Crystal structure of f-NbTe₂ obtained in this work with the detailed configuration of Nb double zig-zag chains in its structure compared to that prepared using the CVT route.

(denoted as f-NbTe₂) is determined, and the crystallographic data are listed in Tables S10-S12. The f-NbTe₂ crystallizes in the monoclinic C2/m space group, similar to that previously reported, but the lattice parameters are refined as a =14.639(7) Å, b = 10.904(4) Å, c = 9.253(4) Å, and $\beta =$ 110.308(16)°, thus resulting in a lattice volume of 1385.1(1) Å³, which is thrice that of C-NbTe₂. Figure 10 shows that in contrast to the chains in $C-NbTe_2$ with equal Nb(1)-Nb(1)distances (3.642 Å), f-NbTe₂ exhibits extra clustering where the trimerization of the Nb atoms occurs along the b-axis. The Nb(1) atoms split into two occupations in f-NbTe2, thus leading to a sequence of two short Nb-Nb distances (3.488 Å), followed by a long Nb-Nb distance (3.928 Å). Consequently, the b-axis is tripled compared to the C-NbTe₂. Reportedly, Te deficiency generally exists in ditelluride crystals prepared via the CVT route.^{70,71} Therefore, we speculate that this new polymorphism of NbTe2 may result from the absence of Te vacancies in the crystals because of the Te-rich synthetic environment used. Considering superconductivity combines with a topological band structure in $C-NbTe_2^{\ 39,40}$ the electronic properties of this polymorph are intriguing and will be investigated in a subsequent study.

CONCLUSIONS

We demonstrated that the alkali metal polytelluride fluxes could lead to the efficient synthesis of new transition metal subtellurides by simply adjusting the ratio between the transition metal and flux. Using a eutectic "K3Te4" polytelluride flux, we arrived at three new ternary compounds, including KNb₃Te₃O_{0.38}, K_{0.9}Nb₃Te₄, and K_{1.06}NbTe₂ in K-Nb-Te system. Among the three, the first two are subtellurides that feature diverse Nb-Nb bonded clusters in the structures. KNb₃Te₃O_{0,38} comprises 1D face-sharing Nb₆ octahedral columns, which are surrounded by Te nets. A peculiar feature in KNb₃Te₃O_{0.38} is the out-of-plane Nb₃triangle clustering in the local range induced by the presence of oxygen between the Nb9 trimers. K0.9Nb3Te4 shows a novel structure with diverse motifs, including 1D Nb-Nb zig-zag chains and unique NbTe4 pyramids, NbTe4 see-saws, and edge-sharing Nb₆ octahedral columns. K_{1.06}NbTe₂ adopts a 2D structure with NbTe6 trigonal-prism layers intercalated by K cations. Furthermore, a new polymorph with extra Nb-Nb clustering was observed in $NbTe_2$. This phase is distinct from that reported by the CVT route.⁴⁴ Using this synthetic method, we were able to control the structural dimensionality and oxidation state by manipulating the composition of the starting materials. This allowed us to synthesize Nb subtellurides with Nb-Nb bonding interactions in a variety of structures. Resistivity measurements and DFT calculations indicated that both $K_{0.9}Nb_3Te_4$ and $K_{1.06}NbTe_2$ show a semimetallic ground state. Conversely, KNb₃Te₃O_{0.38} exhibited semiconductor-like behavior below 29 K, mainly induced by interstitial oxygen. Given the intriguing 1D Nb clusters, potential superconductivity is worthy of investigation in KNb₃Te₃O_{0,38}, especially via physical pressure and chemical doping. High mobility and unusual magnetoresistance can be expected in the K_{0.9}Nb₃Te₄ and K_{1.06}NbTe₂ considering their semimetallic nature with large band dispersions near the Fermi level. The new polytype of NbTe2 also provides a platform for an in-depth understanding of the interactions between charge, spin, and lattice. We anticipate that the eutectic flux technique has the potential to be implemented in other transition metal systems.

ASSOCIATED CONTENT

Supporting Information

The Supporting Information is available free of charge at https://pubs.acs.org/doi/10.1021/acs.inorgchem.3c01621.

Details of the synthesis, structure, and composition determination, resistivity measurements, and DFT functional theory calculations, schematic diagram of the polytelluride flux synthesis, optical photograph, SEM images, EDS, elemental mapping for KNb $_3$ Te $_3$ O $_{0.38}$, K $_{0.9}$ Nb $_3$ Te $_4$, K $_{1.06}$ NbTe $_2$, NbTe $_2$, and NbTe $_4$, PXRD pattern and PDF analysis for KNb $_3$ Te $_3$ O $_{0.38}$, detailed Nb-Nb and Nb-Te bonding distances, refined crystallographic data for KNb $_3$ Te $_3$ O $_{0.38}$, K $_{0.9}$ Nb $_3$ Te $_4$, K $_{1.06}$ NbTe $_2$, and NbTe $_2$ from SCXRD, including Figures S1-S10 and Tables S1-S12 (PDF)

Accession Codes

CCDC 2235758–2235759, 2235767, and 2239730 contain the supplementary crystallographic data for this paper. These data can be obtained free of charge via www.ccdc.cam.ac.uk/data_request/cif, or by emailing data_request/cif, or by contacting The Cambridge Crystallographic Data Centre, 12 Union Road, Cambridge CB2 1EZ, UK; fax: +44 1223 336033.

AUTHOR INFORMATION

Corresponding Authors

Zhongnan Guo — Department of Chemistry, School of Chemistry and Biological Engineering, University of Science and Technology Beijing, Beijing 100083, China; Department of Chemistry, Northwestern University, Evanston, Illinois 60208, United States; orcid.org/0000-0003-4907-4679; Email: guozhongn@ustb.edu.cn

Wenxia Yuan — Department of Chemistry, School of Chemistry and Biological Engineering, University of Science and Technology Beijing, Beijing 100083, China; ⊚ orcid.org/0000-0002-3521-3538; Email: wxyuanwz@163.com

Mercouri G. Kanatzidis — Department of Chemistry, Northwestern University, Evanston, Illinois 60208, United States; Materials Science Division, Argonne National Laboratory, Lemont, Illinois 60439, United States; orcid.org/0000-0003-2037-4168; Email: m-kanatzidis@northwestern.edu

Authors

Fan Sun – Department of Chemistry, School of Chemistry and Biological Engineering, University of Science and Technology Beijing, Beijing 100083, China

Haoyu Yue – Department of Chemistry, School of Chemistry and Biological Engineering, University of Science and Technology Beijing, Beijing 100083, China

Danilo Puggioni – Department of Materials Science and Engineering, Northwestern University, Evanston, Illinois 60208, United States; oorcid.org/0000-0002-2128-4191

Yutong Li – Department of Chemistry, School of Chemistry and Biological Engineering, University of Science and Technology Beijing, Beijing 100083, China

James M. Rondinelli — Department of Materials Science and Engineering, Northwestern University, Evanston, Illinois 60208, United States; Occid.org/0000-0003-0508-2175

Zheng Zhang — School of Materials Science and Engineering, University of Science and Technology Beijing, Beijing 100083, China; orcid.org/0000-0002-9104-7562 Complete contact information is available at: https://pubs.acs.org/10.1021/acs.inorgchem.3c01621

Notes

The authors declare no competing financial interest.

ACKNOWLEDGMENTS

Work conducted at Northwestern University work was supported in part by the National Science Foundation (NSF) (DMR-2305731). Z.G. also acknowledges support from the National Natural Science Foundation of China (grant no. 51832010 and 51872028). Computational work at NU was supported by the National Science Foundation's (NSF) MRSEC program (DMR-1720139) at the Materials Research Center of Northwestern University. Calculations were performed using the Department of Defense High-Performance Computing Modernization Program (DOD-HPCMP). Work conducted at the Argonne National Laboratory was supported by the U.S. Department of Energy, Office of Science, Basic Energy Sciences, Materials Science, and Engineering Division. The use of the Advanced Photon Source (APS) was supported by the U.S. Department of Energy, Office of Science, Office of Basic Energy Sciences under contract no. DE-AC02-06CH11357. We thank Dr. Leighanne Gallington at APS for assisting with our PDF measurements. We also thank Christos D. Malliakas for help with the crystallographic data refinement.

REFERENCES

- (1) Ruck, M. From the metal to the molecule-ternary bismuth subhalides. *Angew. Chem., Int. Ed.* **2001**, *40*, 1182–1193.
- (2) Whangbo, M. H.; Lee, C.; Köhler, J. Metal anions in metal-rich compounds and polar intermetallics. *Eur. J. Inorg. Chem.* **2011**, 2011, 3841–3847.
- (3) Bao, J.-K.; Liu, J.-Y.; Ma, C.-W.; Meng, Z.-H.; Tang, Z.-T.; Sun, Y.-L.; Zhai, H.-F.; Jiang, H.; Bai, H.; Feng, C.-M.; Xu, Z.-A.; Cao, G.-H. Superconductivity in Quasi-One-Dimensional K₂Cr₃As₃ with Significant Electron Correlations. *Phys. Rev. X* **2015**, *5*, 011013.
- (4) Liu, E.; Sun, Y.; Kumar, N.; Muechler, L.; Sun, A.; Jiao, L.; Yang, S.-Y.; Liu, D.; Liang, A.; Xu, Q.; Kroder, J.; Süß, V.; Borrmann, H.; Shekhar, C.; Wang, Z.; Xi, C.; Wang, W.; Schnelle, W.; Wirth, S.; Chen, Y.; Goennenwein, S. T. B.; Felser, C. Giant anomalous Hall effect in a ferromagnetic kagome-lattice semimetal. *Nat. Phys.* 2018, 14, 1125–1131.
- (\$) Liu, D. F.; Liang, A. J.; Liu, E. K.; Xu, Q. N.; Li, Y. W.; Chen, C.; Pei, D.; Shi, W. J.; Mo, S. K.; Dudin, P.; Kim, T.; Cacho, C.; Li, G.; Sun, Y.; Yang, L. X.; Liu, Z. K.; Parkin, S. S. P.; Felser, C.; Chen, Y. L. Magnetic Weyl semimetal phase in a Kagomé crystal. *Science* 2019, 365, 1282–1285.
- (6) Shen, J.; Yao, Q.; Zeng, Q.; Sun, H.; Xi, X.; Wu, G.; Wang, W.; Shen, B.; Liu, Q.; Liu, E. Local Disorder-Induced Elevation of Intrinsic Anomalous Hall Conductance in an Electron-Doped Magnetic Weyl Semimetal. *Phys. Rev. Lett.* **2020**, *125*, 086602.
- (7) Ali, M. N.; Xiong, J.; Flynn, S.; Tao, J.; Gibson, Q. D.; Schoop, L. M.; Liang, T.; Haldolaarachchige, N.; Hirschberger, M.; Ong, N. P.; Cava, R. J. Large, non-saturating magnetoresistance in WTe₂. *Nature* **2014**, *514*, 205–208.
- (8) Soluyanov, A. A.; Gresch, D.; Wang, Z.; Wu, Q.; Troyer, M.; Dai, X.; Bernevig, B. A. Type-II Weyl semimetals. *Nature* **2015**, *527*, 495–498.
- (9) Khoury, J. F.; Rettie, A. J. E.; Khan, M. A.; Ghimire, N. J.; Robredo, I.; Pfluger, J. E.; Pal, K.; Wolverton, C.; Bergara, A.; Jiang, J. S.; Schoop, L. M.; Vergniory, M. G.; Mitchell, J. F.; Chung, D. Y.; Kanatzidis, M. G. A New Three-Dimensional Subsulfide Ir₂In₈S with Dirac Semimetal Behavior. *J. Am. Chem. Soc.* **2019**, *141*, 19130–19137.

- (10) Khoury, J. F.; Rettie, A. J. E.; Robredo, I.; Krogstad, M. J.; Malliakas, C. D.; Bergara, A.; Vergniory, M. G.; Osborn, R.; Rosenkranz, S.; Chung, D. Y.; Kanatzidis, M. G. The Subchalcogenides ${\rm Ir_2In_8Q}$ (Q = S, Se, Te): Dirac Semimetal Candidates with Reentrant Structural Modulation. *J. Am. Chem. Soc.* **2020**, *142*, 6312–6323.
- (11) Gibson, Q. D.; Schoop, L. M.; Muechler, L.; Xie, L. S.; Hirschberger, M.; Ong, N. P.; Car, R.; Cava, R. Three-dimensional Dirac semimetals: Design principles and predictions of new materials. *Phys. Rev. B: Condens. Matter Mater. Phys.* **2015**, *91*, 205128.
- (12) Nakayama, K.; Wang, Z.; Trang, C. X.; Souma, S.; Rienks, E. D. L.; Takahashi, T.; Ando, Y.; Sato, T. Observation of Dirac-like energy band and unusual spectral line shape in quasi-one-dimensional superconductor Tl₂Mo₆Se₆. *Phys. Rev. B* **2018**, *98*, 140502.
- (13) Bao, J.-K.; Tang, Z.-T.; Jung, H. J.; Liu, J.-Y.; Liu, Y.; Li, L.; Li, Y.-K.; Xu, Z.-A.; Feng, C.-M.; Chen, H.; Chung, D. Y.; Dravid, V. P.; Cao, G. H.; et al. Unique [Mn₆Bi₅] Nanowires in KMn₆Bi₅: A Quasi-One-Dimensional Antiferromagnetic Metal. *J. Am. Chem. Soc.* **2018**, 140, 4391–4400.
- (14) Liu, Z. Y.; Dong, Q. X.; Yang, P. T.; Shan, P. F.; Wang, B. S.; Sun, J. P.; Dun, Z. L.; Uwatoko, Y.; Chen, G. F.; Dong, X. L.; Zhao, Z. X.; Cheng, J.-G. Pressure-induced superconductivity up to 9 K in the quasi-one-dimensional KMn_KBi₅. *Phys. Rev. Lett.* **2022**, *128*, 187001.
- (15) Yin, J.-X.; Zhang, S. S.; Chang, G.; Wang, Q.; Tsirkin, S. S.; Guguchia, Z.; Lian, B.; Zhou, H.; Jiang, K.; Belopolski, I.; Shumiya, N.; Multer, D.; Litskevich, M.; Cochran, T. A.; Lin, H.; Wang, Z.; Neupert, T.; Jia, S.; Lei, H.; Hasan, M. Z. Negative flat band magnetism in a spin-orbit-coupled correlated kagome magnet. *Nat. Phys.* **2019**, *15*, 443–448.
- (16) Ortiz, B. R.; Teicher, S. M. L.; Hu, Y.; Zuo, J. L.; Sarte, P. M.; Schueller, E. C.; Abeykoon, A. M. M.; Krogstad, M. J.; Rosenkranz, S.; Osborn, R.; Seshadri, R.; Balents, L.; He, J.; Wilson, S. D. CsV₃Sb₅: a Z₂ topological kagome metal with a superconducting ground state. *Phys. Rev. Lett.* **2020**, *125*, 247002.
- (17) Nie, L.; Sun, K.; Ma, W.; Song, D.; Zheng, L.; Liang, Z.; Wu, P.; Yu, F.; Li, J.; Shan, M.; Zhao, D.; Li, S.; Kang, B.; Wu, Z.; Zhou, Y.; Liu, K.; Xiang, Z.; Ying, J.; Wang, Z.; Wu, T.; Chen, X. Chargedensity-wave-driven electronic nematicity in a kagome superconductor. *Nature* **2022**, *604*, 59–64.
- (18) Han, G. H.; Duong, D. L.; Keum, D. H.; Yun, S. J.; Lee, Y. H. van der Waals metallic transition metal dichalcogenides. *Chem. Rev.* **2018**, *118*, 6297–6336.
- (19) Li, G.; Xu, Q.; Shi, W.; Fu, C.; Jiao, L.; Kamminga, M. E.; Yu, M.; Tüysüz, H.; Kumar, N.; Süß, V.; Saha, R.; Srivastava, A. K.; Wirth, S.; Auffermann, G.; Gooth, J.; Parkin, S.; Sun, Y.; et al. Surface states in bulk single crystal of topological semimetal $\text{Co}_3\text{Sn}_2\text{S}_2$ toward Water oxidation. *Sci. Adv.* **2019**, *5*, No. eaaw9867.
- (20) Zhao, L. D.; Lo, S. H.; Zhang, Y.; Sun, H.; Tan, G.; Uher, C.; Wolverton, C.; Dravid, V. P.; Kanatzidis, M. G. Ultralow thermal conductivity and high thermoelectric figure of merit in SnSe crystals. *Nature* **2014**, *508*, 373–377.
- (21) Sim, Y.; Yoon, A.; Kang, H. S.; Kwak, J.; Kim, S. Y.; Jo, Y.; Choe, D.; Na, W.; Lee, M. H.; Park, S. D.; Song, S.; Kim, D.; Yoo, J.; Kim, S. Y.; Cheong, H.; Lee, J. S.; Lee, C. H.; Lee, Z.; Kwon, S. Y. Design of 2D layered catalyst by coherent heteroepitaxial conversion for robust hydrogen generation. *Adv. Funct. Mater.* **2021**, *31*, 2005449.
- (22) Wang, P. L.; Liu, Z.; Chen, P.; Peters, J. A.; Tan, G.; Im, J.; Lin, W. W.; Freeman, A. J.; Wessels, B. W.; Kanatzidis, M. G. Hard radiation detection from the selenophosphate Pb₂P₂Se₆. *Adv. Funct. Mater.* **2015**, 25, 4874–4881.
- (23) Hönle, W.; Von Schnering, H. G.; Lipka, A.; Yvon, K. New compounds with infinite chains of face-condensed octahedral Mo₆ clusters: InMo₃Se₃, InMo₃Te₃, TlMo₃Se₃ and TlMo₃Te₃. *J. Less-Common Met.* **1980**, 71, 135–145.
- (24) Hor, P. H.; Fan, W. C.; Chou, L. S.; Meng, R. L.; Chu, C. W.; Tarascon, J. M.; Wu, M. K. Study of the metal-semiconductor transition in Rb₂Mo₆Se₆, Rb₂Mo₆Te₆ and Cs₂Mo₆Te₆ under pressures. *Solid State Commun.* **1985**, *55*, 231–235.

- (25) Amberger, E.; Polborn, K.; Grimm, P.; Dietrich, M.; Obst, B. Superconductivity in the Nb cluster compounds $Nb_3(X, Y)_4$ with X, Y = S, Se, Te. *Solid State Commun.* **1978**, *26*, 943–947.
- (26) Sokolikova, M. S.; Mattevi, C. Direct synthesis of metastable phases of 2D transition metal dichalcogenides. *Chem. Soc. Rev.* **2020**, 49, 3952–3980.
- (27) Su, J. W.; Liu, K. L.; Wang, F. K.; Jin, B.; Guo, Y. B.; Liu, G. H.; Li, H. Q.; Zhai, T. Y. van der Waals 2D transition metal tellurides. *Adv. Mater. Interfac.* **2019**, *6*, 1900741.
- (28) Kanatzidis, M. G.; Pöttgen, R.; Jeitschko, W. The metal flux: a preparative tool for the exploration of intermetallic compounds. *Angew. Chem., Int. Ed.* **2005**, 44, 6996–7023.
- (29) Kanatzidis, M.; Sun, H. Z.; Dehnen, S. Bismuth—The Magic Element. *Inorg. Chem.* **2020**, *59*, 3341–3343.
- (30) Wang, J.; Yang, M.; Pan, M.-Y.; Xia, S.-Q.; Tao, X.-T.; He, H.; Darone, G.; Bobev, S. Synthesis Crystal and Electronic Structures, and Properties of the New Pnictide Semiconductors A₂CdPn₂ (A = Ca, Sr, Ba, Eu; Pn = P, As). *Inorg. Chem.* **2011**, *50*, 8028–8037.
- (31) Latturner, S. E. Clusters, Assemble: Growth of Intermetallic Compounds from Metal Flux Reactions. *Acc. Chem. Res.* **2018**, *51*, 40–48.
- (32) Benavides, K. A.; Oswald, I. W. H.; Chan, J. Y. Casting a Wider Net: Rational Synthesis Design of Low-Dimensional Bulk Materials. *Acc. Chem. Res.* **2018**, *51*, 12–20.
- (33) Zhou, X.; Kolluru, V. S. C.; Xu, W.; Wang, L.; Chang, T.; Chen, Y.-S.; Yu, L.; Wen, J.; Chan, M. K. Y.; Chung, D. Y.; Kanatzidis, M. G. Discovery of Chalcogenides Structures and Compositions Using Mixed Fluxes. *Nature* **2022**, *612*, 72–77.
- (34) Zhou, X.; Mandia, D. J.; Park, H.; Balasubramanian, M.; Yu, L.; Wen, J.; Yakovenko, A.; Chung, D. Y.; Kanatzidis, M. G. New compounds and phase selection of nickel sulfides via oxidation state control in molten hydroxides. *J. Am. Chem. Soc.* **2021**, *143*, 13646–13654.
- (35) Zhou, X.; Malliakas, C. D.; Yakovenko, A. A.; Wilfong, B.; Wang, S. G.; Chen, Y. S.; Yu, L.; Wen, J.; Balasubramanian, M.; Wang, H.-H.; Chung, D. Y.; Kanatzidis, M. G. Coherent Approach to Two-Dimensional Heterolayered Oxychalcogenides Using Molten Hydroxides. *Nat. Synth.* **2022**, *1*, 729–737.
- (36) Kanatzidis, M. G. New directions in synthetic solid state chemistry: chalcophosphate salt fluxes for discovery of new multinary solids. *Curr. Opin. Solid State Mater. Sci.* **1997**, *2*, 139–149.
- (37) Matsushita, Y.; Kanatzidis, M. G. Synthesis and Structure of Li₄GeS₄. Z. Naturforsch., B: J. Chem. Sci. 1998, 53, 23-30.
- (38) Kanatzidis, M. G. Discovery-synthesis, design, and prediction of chalcogenide phases. *Inorg. Chem.* **2017**, *56*, 3158–3173.
- (39) Nagata, S.; Abe, T.; Ebisu, S.; Ishihara, Y.; Tsutsumi, K. Superconductivity in the metallic layered compound NbTe₂. *J. Phys. Chem. Solids* **1993**, *54*, 895–899.
- (40) Tang, F.; Po, H. C.; Vishwanath, A.; Wan, X. Comprehensive search for topological materials using symmetry indicators. *Nature* **2019**, *566*, 486–489.
- (41) De Lima, B. S.; Chaia, N.; Correa, L. E.; Oliveira, F. S.; de Faria, L. R.; de Oliveira, I.; Coelho, G. C.; Machado, A. J. S. Experimental Study of the Binary Nb-Te System. *J. Phase Equilib. Diffus.* **2019**, *40*, 697–705.
- (42) Selte, K.; Kjekshus, A.; Ewing, V.; Hedberg, K.; Trætteberg, M. Crystal Structures of Nb₅Se₄ and Nb₅Te₄. *Acta Chem. Scand.* **1963**, *17*, 2560–2562.
- (43) Selte, K.; Kjekshus, A. The crystal structures of Nb₃Se₄ and Nb₃Te₄. *Acta Crystallogr.* **1964**, *17*, 1568–1572.
- (44) Brown, B. E. The crystal structures of NbTe₂ and TaTe₂. Acta Crystallogr. 1966, 20, 264–267.
- (45) Selte, K.; Kjekshus, A.; Petersen, C. S.; Halvarson, H.; Nilsson, L. On the crystal structure of NbTe₄. *Acta Chem. Scand.* **1964**, *18*, 690–696
- (46) Cannon, J. F.; Robertson, D. L.; Hall, H. T.; Lawson, A. C. High-pressure synthesis of β -W-type Nb₃Te. *J. Phys. Chem. Solids* **1974**, *15*, 1181–1182.

- (47) Huan, G.; Greenblatt, M. New $A_xNb_oSe_8$ (A= Na, K, Rb, Cu, Ag, Zn, Cd, Pb) phases with the Nb_3Te_4 structure. *Mater. Res. Bull.* 1987, 22, 505–512.
- (48) Bale, C. W.; Bélisle, E.; Chartrand, P.; Decterov, S. A.; Eriksson, G.; Gheribi, A. E.; Hack, K.; Jung, I. H.; Kang, Y. B.; Melancon, J.; Pelton, A. D.; Petersen, S.; Robelin, C.; Sangster, J.; Spencer, P.; Van Ende, M. A. FactSage thermochemical software and databases, 2010-2016. *Calphad* **2016**, *54*, 35–53.
- (49) Klepp, K.; Boller, H. Die Kristallstruktur von TlFe₃Te₃. Monatsh. Chem. **1979**, 110, 677–684.
- (50) Sun, F.; Guo, Z. N.; Liu, N.; Wu, D.; Lin, J. W.; Cheng, E. J.; Ying, T. P.; Li, S. Y.; Yuan, W. X. Cs_{0.9}Ni_{3.1}Se₃: A Ni-Based Quasi-One-Dimensional Conductor with Spin-Glass Behavior. *Inorg. Chem.* **2018**, *57*, 3798–3804.
- (51) Wu, E. J.; Pell, M. A.; Genin, H. S.; Ibers, J. A. Synthesis, characterization, and electronic structure of KV₃Te₃O_{0.42}. *J. Alloys Compd.* **1998**, 278, 123–129.
- (52) Guo, Z. N.; Sun, F.; Puggioni, D.; Luo, Y. B.; Li, X. T.; Zhou, X. Q.; Chung, D. Y.; Cheng, E. J.; Li, S. Y.; Rondinelli, M.; Yuan, W. X.; Kanatzidis, M. G. Local Distortions and Metal—Semiconductor—Metal Transition in Quasi-One-Dimensional Nanowire Compounds $AV_3Q_3O_\delta$ (A= K, Rb, Cs and Q= Se, Te). *Chem. Mater.* **2021**, 33, 2611–2623.
- (53) Simon, A. Condensed Metal Clusters. Angew. Chem., Int. Ed. 1981, 20, 1-22.
- (54) Simon, A. Clusters of Valence Electron Poor Metals-Structure, Bonding, and Properties. *Angew. Chem., Int. Ed.* **1988**, 27, 159–183.
- (55) Lokken, D. A.; Corbett, J. D. Gadolinium sesquichloride, an unusual example of metal-metal bonding. *J. Am. Chem. Soc.* **1970**, 92, 1799–1800.
- (56) Torardi, C. C.; McCarley, R. E. Sodium tetramolybdenum hexoxide (NaMo₄O₆). A metallic infinite-chain polymer derived by condensation of octahedral clusters. *J. Am. Chem. Soc.* **1979**, *101*, 3963–3964.
- (57) Zhao, J.; Islam, S. M.; Hao, S. Q.; Tan, G. J.; Stoumpos, C. C.; Wolverton, C.; Chen, H. J.; Luo, Z. Z.; Li, R. K.; Kanatzidis, M. G. Homologous Series of 2D Chalcogenides Cs-Ag-Bi-Q (Q= S, Se) with Ion-Exchange Properties. *J. Am. Chem. Soc.* **2017**, *139*, 12601–12609.
- (58) Zhao, J.; Islam, S. M.; Kontsevoi, O. Y.; Tan, G. J.; Stoumpos, C. C.; Chen, H. J.; Li, R. K.; Kanatzidis, M. G. The Two-Dimensional $A_xCd_xBi_{4-x}Q_6$ (A= K, Rb, Cs; Q= S, Se): Direct Bandgap Semiconductors and Ion-Exchange Materials. *J. Am. Chem. Soc.* **2017**, *139*, 6978–6987.
- (59) Sankar, R.; Narsinga Rao, G.; Muthuselvam, I. P.; Butler, C.; Kumar, N.; Senthil Murugan, G.; Shekhar, C.; Chang, T. R.; Wen, C. Y.; Chen, C. W.; Lee, W. L.; Lin, M. T.; Jeng, H. T.; Felser, C.; Chou, F. C. Polymorphic Layered MoTe₂ from Semiconductor, Topological Insulator, to Weyl Semimetal. *Chem. Mater.* **2017**, *29*, 699–707.
- (60) Canadell, E.; Jobic, S.; Brec, R.; Rouxel, J.; Whangbo, M. H. Importance of short interlayer Te. Te contacts for the structural distortions and physical properties of CdI₂-type layered transitionmetal ditellurides. *J. Solid State Chem.* **1992**, *99*, 189−199.
- (61) Corbett, J. D. Exploratory Synthesis in the Solid State. Endless Wonders. *Inorg. Chem.* **2000**, *39*, 5178–5191.
- (62) Corbett, J. D.; Garcia, E.; Guloy, A. M.; Hurng, W.-M.; Kwon, Y.-U.; Leon-Escamilla, E. A. Widespread interstitial chemistry of Mn₅Si₃-Type and related phases. Hidden impurities and opportunities. *Chem. Mater.* **1998**, *10*, 2824–2836.
- (63) Henning, R. W.; Leon-Escamilla, E. A.; Zhao, J.-T.; Corbett, J. D. Stabilization by hydrogen. Synthetic and structural studies of the Zintl phase $Ba_5Ga_6H_2$. *Inorg. Chem.* **1997**, *36*, 1282–1285.
- (64) Leon-Escamilla, E. A.; Corbett, J. D. Hydrogen impurity effects. A_5 Tt₃ intermetallic compounds between A = Ca, Sr, Ba, Eu and Tt = Si, Ge, Sn with Cr_5B_3 -like structures that are stable both as binary and as ternary hydride and fluoride phases. *J. Solid State Chem.* **2001**, *159*, 149–162.

- (65) Baber, W. G. The contribution to the electrical resistance of metals from collisions between electrons. *Proc.: Math., Phys. Eng. Sci.* 1937, 158, 0383–0396.
- (66) Deringer, V. L.; Tchougréeff, A. L.; Dronskowski, R. Crystal orbital hamilton population (COHP) analysis as projected from plane-wave basis sets. *J. Phys. Chem. A* **2011**, *115*, 5461–5466.
- (67) Maintz, S.; Deringer, V. L.; Tchougréeff, A. L.; Dronskowski, R. LOBSTER: A tool to extract chemical bonding from plane-wave based DFT. *J. Comput. Chem.* **2016**, *37*, 1030–1035.
- (68) Maintz, S.; Esser, M.; Dronskowski, R. Efficient rotation of local basis functions using real spherical harmonics. *Acta Phys. Pol., B* **2016**, 47, 1165–1175.
- (69) Maintz, S.; Deringer, V. L.; Tchougréeff, A. L.; Dronskowski, R. Analytic projection from plane-wave and PAW wavefunctions and application to chemical-bonding analysis in solids. *J. Comput. Chem.* **2013**, *34*, 2557–2567.
- (70) Chen, H. X.; Li, Z. L.; Fan, X.; Guo, L. W.; Chen, X. L. Quantum linear magnetoresistance in NbTe₂. Solid State Commun. **2018**, 275, 16–20.
- (71) Sörgel, T.; Nuss, J.; Wedig, U.; Kremer, R. K.; Jansen, M. A new low-temperature modification of TaTe₂—comparison to the room temperature and the hypothetical 1T-TaTe₂ modification. *Mater. Res. Bull.* **2006**, *41*, 987–1000.